PHYSICAL REVIEW B **111**, 085424 (2025)

Interlayer excitons in double-layer transition metal dichalcogenide quantum dots

Xiang Liu,[1] Zheng Tao,[1] Wenchen Luo,[1,*] and Tapash Chakraborty[2]
[1]School of Physics, Central South University, Changsha 410083, China
[2]Department of Physics and Astronomy, University of Manitoba, Winnipeg, Canada R3T 2N2

(Received 14 August 2024; revised 5 February 2025; accepted 7 February 2025; published 21 February 2025)

Various properties of interlayer excitons in double-layer transition metal dichalcogenide quantum dots are analyzed using a low-energy effective Hamiltonian with Coulomb interaction. We analytically solve the single-particle Hamiltonian with and without a magnetic field, then present the electron-hole pairing features of interlayer excitons by employing the exact-diagonalization technique, where the electron and hole are located in two layers, respectively. In a magnetic field, the Landau-level gap, as well as the electron-hole separation of an exciton, varies nonmonotonously as the interlayer distance increases, which is attributed to the pseudo-spin-orbit coupling that also leads to the emergence of topological nontrivial pseudospin textures in the exciton states. We examine the influence of different materials in quantum dots stacking on the exciton states, comparing their impact to variations in layer distances and quantum dot sizes. We further explore two interacting interlayer excitons numerically. The binding energy is significantly enhanced by the exchange interaction when the two electrons have different spins. The optical absorption spectra from the ground state to low-lying excited states reveal distinct behaviors for different interlayer excitons, which can be utilized to distinguish the spin of electrons in excitons. Our results highlight the potential for controlling interlayer excitons and applications of optical devices in a magnetic field and tunable layer distance.

DOI: 10.1103/PhysRevB.111.085424

I. INTRODUCTION

Interlayer excitons form when an electron and a hole with strong mutual Coulomb interaction are localized in different monolayers. Recently, this emerging phenomenon has received increasing attention, prompting extensive theoretical and experimental studies, particularly within transition metal dichalcogenides (TMDs) [1,2]. TMDs are a novel family of two-dimensional (2D) materials with unique optoelectronic properties and are highly useful in various fields, including optoelectronic device, energy, and medical applications [3,4]. These materials, described by the formula MX_2 ($M =$ Mo, W and $X =$ S, Se) [5], are distinguished from graphene by their strong spin-orbit couplings (SOCs) originating from heavy transition metal atoms [6,7]. In contrast to their bulk counterparts, monolayer TMDs have a direct band gap of about 2 eV, making them attractive for optical studies and applications. Most heterostructures exhibit a type-II band alignment under specific conditions, where the conduction band minimum (CBM) and valence band maximum (VBM) lie in different layers [8–10]. Alternatively, voltage modulation can also be used to form the type-II band alignment [11,12]. These heterostructures facilitate the formation of interlayer excitons and provide a versatile platform for exploring correlated electronic states, paving the way for novel optical and electronic phenomena [13]. Recent works on interlayer excitons in TMDs have revealed different behavior from intralayer excitons, particularly that the lifetime of an interlayer exciton can be up to two orders of magnitude longer than that of an intralayer exciton [14–18].

Excitons in bilayer two-dimensional electron systems have, of late, garnered significant interest, which supports supercurrent, excitonic superfluidity, novel crystal phases, interlayer exciton polarons, etc. [19–24]. The heterostructures, including both homobilayers (made from the same TMDs) and heterobilayers (made from different TMDs) [25], and hybrid heterostructures combining perovskite and TMDs have been recently fabricated [26–28]. These stacking structures have been extensively researched for their optoelectronic properties and applications, which underscores the primary focus of our study.

The confined nanostructures such as quantum dots (QDs) and quantum rings based on semiconductor heterostructures were extensively investigated and were also utilized in optical devices [29–32]. The optical absorption spectra in a parabolic QD, first studied theoretically in Ref. [33], were in excellent agreement with the observed low-energy emission lines in a subsequent experiment [34]. Theories and experiments on electrons in elliptical and circular QDs have displayed fascinating optical and transport properties influenced by confinement effects, focusing on both single-particle and few-body systems. Numerous studies on graphene and TMDs demonstrate various techniques for implementing QDs in 2D materials, which paves the way for exploring and applying these artificial atoms with novel electronic and optical properties [32,35–41], in comparison to the QDs in conventional semiconductors. Electrons trapped in bilayer and trilayer graphene QDs have been studied numerically by using the finite-element method, where interlayer coupling is considered [36,42]. The QD located in a monolayer TMD nanoflake can also be experimentally achieved and are theoretically studied [43–49].

---

[*] Contact author: luo.wenchen@csu.edu.cn

©2025 American Physical Society

Motivated by the vast application potential of TMDs, in the present work, we explore interlayer excitons by constructing a double QD structure based on TMDs, where electrons and holes are located in different layers. Between the two layers, aside from the Coulomb interactions, the particle hopping across different layers is disregarded. The distance of the two layers and an external magnetic field is externally adjustable. We investigate how the layer distance and the magnetic field influence the properties of interlayer excitons within the double-layer QDs. Recent studies of TMDs under out-of-plane magnetic fields of up to 31 T highlight their impact on exciton behaviors [50]. Our device based on TMDs would be ideal for studying its optical and transport properties. This system with strong Coulomb interactions is also promising for studying electron-hole pairing and enhancing the understanding of correlated electronic states [51,52].

The manuscript is organized as follows. In Sec. II, we present our model for electron-hole pairs in double TMD QDs, including the Hamiltonian formalism and a review of single-particle solutions within the TMD QDs. We then introduce the interlayer Coulomb interaction matrix elements used for the numerical analyses. To streamline the discussion, we address the Coulomb interaction matrix elements separately in the absence and presence of an external magnetic field. In Sec. III, we employ the exact-diagonalization (ED) techniques to calculate the ground-state and low-lying excited energies, electron-hole separation, and optical absorption strengths of interlayer excitons for double TMD QDs. Additionally, the discussion encompasses the topological properties of an interlayer exciton. In Sec. IV, the results of biexciton are discussed, where the exciton-exciton interaction plays an important role. In Sec. V, we present a summary and outlook on the exciton features.

II. MODEL HAMILTONIAN

In our model, two monolayer TMDs are positioned in the upper and lower planes, respectively, and are separated by a hexagonal boron nitride (hBN) substrate [16,53]. For each TMD layer, the single-particle behavior in the vicinity of the K/K' points is described by the widely adopted gapped Dirac Hamiltonian, especially in the low-energy region [6,7]. This study focuses on the impact of Coulomb interactions on exciton formation within the QDs. Recent studies employ the periodic moiré potential in moiré superlattices to form quantum dot arrays [35,51,54]. However, we construct a double QD structure confining electrons and holes in different monolayers, respectively, by using an infinite potential without twist. The advantage of our approach is that it allows for convenient transport measurements and the study of optical properties with minimal interference. In this work, we focus on interlayer excitons with long-range Coulomb interaction and ignore hopping between the layers given that the distance of the two layers is relatively large. The conduction and valence bands thus remain approximately unchanged. The system is described by the Hamiltonian

$$H = H_e + H_h + H_{eh} + H_{ee} + H_{hh}, \tag{1}$$

where H_e and H_h, respectively, correspond to the single-particle Hamiltonian in the upper and lower layer QDs, H_{eh} is the Coulomb interaction between the electron and the hole located in different layers, H_{ee} describes the intralayer electron-electron interaction, and H_{hh} is the intralayer hole-hole interaction. Without loss of generality, we suppose that electrons are in the upper QD and holes are located in the lower QD.

The Hamiltonian of the single particle in a TMD QD is

$$H_\zeta = \frac{a_\zeta t_\zeta}{\hbar} H_\tau + \frac{\Delta_\zeta}{2}\sigma_z + \frac{\lambda_\zeta \tau s}{2}(1-\sigma_z) + V(\mathbf{r}_\zeta)\sigma_z, \tag{2}$$

where $\zeta = e, h$ denotes the index of the electron or hole layer, a_ζ is the lattice constant of the TMDs of the layer, t_ζ is the hopping parameter, τ is the valley index that is ± 1 for the K and K' valley, respectively, σ_z is a Pauli matrix representing the sublattice pseudospin, $H_\tau = \tau\sigma_x(p_x + eA_x) + \sigma_y(p_y + eA_y)$ with vector potential $\mathbf{A} = (A_x, A_y)$ in a perpendicular magnetic field represents the sublattice pseudo-SOC, Δ is the energy gap between the valence and conduction bands, λ is a constant coupling the spin and valley, $s = \pm 1$ represents spin up and spin down acting as a good quantum number, respectively, and $\boldsymbol{r}_{e(h)}$ are the position vectors in different layers. Given that the Fermi velocity t_ζ can be different in different bands, the effective masses of the electron and the hole could be different. The small spin-splitting energy and the Zeeman term are not explicitly shown in Eq. (2) since it is not related to the binding energy of an exciton.

The QD can be produced by cutting a monolayer TMD nanoflake of radius R or lateral confinement potential on an extended monolayer [43–47]. Then we adopt the infinite mass boundary [55] for the QD,

$$V(\mathbf{r}) = \begin{cases} 0, & r < R \\ \infty, & r > R, \end{cases} \tag{3}$$

which allows us to obtain exact solutions of single-particle wave functions. To solve the many-particle system, we should first establish the single-particle eigenstates of the noninteracting Hamiltonian as the basis. The solutions of the single-particle Hamiltonian are given in the following.

A. Wave functions without a magnetic field

In the absence of a magnetic field, the wave function is an eigenstate of the total angular momentum operator $J_{\text{tot}} = L_z + \tau\frac{\hbar\sigma_z}{2}$ since it commutes with the Hamiltonian $[J_{\text{tot}}, H_\zeta] = 0$, where $L_z = xp_y - yp_x$ is the z component of the angular momentum. Given that the spin is a good quantum number, we start from the eigenvalue equation $H_\zeta\Psi_\zeta = E_\zeta\Psi_\zeta$ for spin s in polar coordinate (r,θ) with the wave function being a two-component spinor. Consider that in either the upper or lower layer, the eigenvalues equations are the same in form. We drop the layer index in this section, unless otherwise specified. The wave function should be labeled by four indices, i.e., principal quantum number n, angular momentum j, valley τ, and spin s. For simplicity, the wave function spinor, without the four indices, can be written as

$$\psi(r,\theta) = \begin{pmatrix} e^{i(j-\frac{\tau}{2})\theta}\chi_1(r) \\ ie^{i(j+\frac{\tau}{2})\theta}\chi_2(r) \end{pmatrix}, \tag{4}$$

where the total angular momentum quantum number $j = m + \frac{\tau}{2}$ with orbital angular momentum quantum number

$m = 0, \pm 1, \pm 2, \dots$, while $\chi_1(r)$ and $\chi_2(r)$ are the radial wave functions that are the envelope functions containing the principal quantum number n. The eigenstate problem can be written as two coupled differential equations for the two spinor components,

$$at\left(\tau\nabla_r + \frac{j+\frac{\tau}{2}}{r}\right)\chi_2(r) = \left(-\frac{\Delta}{2} + E_j\right)\chi_1(r), \tag{5}$$

$$at\left(\tau\nabla_r - \frac{j-\frac{\tau}{2}}{r}\right)\chi_1(r) = \left(\lambda\tau s - \frac{\Delta}{2} - E_j\right)\chi_2(r), \tag{6}$$

where E_j is the eigenenergy with total angular momentum quantum number j. Following a series of mathematical steps (see Appendix B for detailed derivations), we obtain the single-particle wave function,

$$\psi = N\begin{pmatrix} e^{i(j-\frac{\tau}{2})\theta}\frac{2at}{2E_j-\Delta}\sqrt{\kappa_j}\varrho J_{(j-\frac{\tau}{2})}(\sqrt{\kappa_j}r) \\ ie^{i(j+\frac{\tau}{2})\theta}\varrho J_{(j+\frac{\tau}{2})}(\sqrt{\kappa_j}r) \end{pmatrix}, \tag{7}$$

where N is the normalization coefficient, J is a Bessel function of the first kind, and we define $\kappa_j = (2E_j - \Delta)(2E_j + \Delta - 2\tau s\lambda)/4a^2t^2$. Here, ϱ assumes distinct values corresponding to the various angular momentum quantum states. The infinite mass boundary condition implies that the eigenvalue equations satisfy

$$\chi_2(R) = i\tau\chi_1(R) \tag{8}$$

at the border of the QD [55–59]. Through numerical solutions of the boundary condition in Eq. (8), one can determine a series of energies at the angular momentum j marked as $E_{n,j}$ labeled by quantum number n. Consequently, the energy spectrum of the QD is obtained at zero magnetic field.

B. Wave functions in the presence of a magnetic field

We now proceed to solve the wave functions in a homogeneous perpendicular magnetic field B. In this case, the Hamiltonian also takes the form of Eq. (2). We derive a pair of coupled differential equations for a two-component spinor in the presence of a magnetic field,

$$\left(\tau\nabla_\rho + \frac{j+\frac{\tau}{2}}{\rho} + \beta\rho\right)\chi_2(\rho) = \left(\varepsilon - \frac{1}{2}\delta\right)\chi_1(\rho) \tag{9a}$$

$$\left(\tau\nabla_\rho - \frac{j-\frac{\tau}{2}}{\rho} - \beta\rho\right)\chi_1(\rho) = \left(\Lambda\tau s - \frac{1}{2}\delta - \varepsilon\right)\chi_2(\rho), \tag{9b}$$

where we define a series of dimensionless parameters, $\rho = \frac{r}{a}$, $\beta = \frac{eB}{2\hbar}a^2$, $\varepsilon = \frac{E}{t}$, $\delta = \frac{\Delta}{t}$, and $\Lambda = \frac{\lambda}{t}$. Using the same steps as mentioned in the last section, we substitute Eq. (9b) into Eq. (9a), and make an ansatz $\chi_1(\rho) = \rho^{|j-\frac{\tau}{2}|}\exp(-\frac{\beta\rho^2}{2})\chi_0(\rho)$. Then a confluent hypergeometric equation is obtained,

$$x\nabla_x^2\chi_0(x) + (b - x)\nabla_x\chi_0(x) - \alpha\chi_0(x) = 0, \tag{10}$$

where we define $x = \beta\rho^2$, $b = |j - \frac{\tau}{2}| + 1$, and

$$\alpha = \frac{1}{2}\left(j + \frac{\tau}{2} + b\right) - \frac{\left(\varepsilon + \frac{1}{2}\delta - \Lambda\tau s\right)\left(\varepsilon - \frac{1}{2}\delta\right)}{4\beta}. \tag{11}$$

After some algebraic operations, we obtain the single-particle eigenstate in the presence of an external magnetic field,

$$\psi = N\begin{pmatrix} e^{i(j-\frac{\tau}{2})\theta}\rho^{|j-\frac{\tau}{2}|}\exp\left(-\frac{\beta\rho^2}{2}\right){}_1F_1(\alpha, b, \beta\rho^2) \\ ie^{i(j+\frac{\tau}{2})\theta}\rho^{|j-\frac{\tau}{2}|-1}\exp\left(-\frac{\beta\rho^2}{2}\right)\gamma\Gamma(\rho) \end{pmatrix}, \tag{12}$$

where N is the normalization constant and ${}_1F_1(\alpha, b, r)$ is the confluent hypergeometric function. Here, we define $\Gamma(\rho) = \xi{}_1F_1(\alpha, b, \beta\rho^2) + \tau\frac{2\alpha}{b}\beta\rho^2{}_1F_1(\alpha+1, b+1, \beta\rho^2)$ with $\xi = \tau|j - \frac{\tau}{2}| - j + \frac{\tau}{2} - (\tau+1)\beta\rho^2$ and $\gamma = -(\varepsilon + \frac{1}{2}\delta - \Lambda\tau s)^{-1}$. Again, using the infinite mass boundary condition in Eq. (8), we can numerically determine the energy spectrum [32,55–59].

C. Many-body Hamiltonian

Once the single-particle wave functions are obtained, we can construct the generic many-body basis as $|i\rangle \equiv |i_{e_1}, \dots i_{e_{N_e}}; i_{h_1}, \dots, i_{h_{N_h}}\rangle$, which contains N_e electrons and N_h holes. Each i_{e_k} and i_{h_k} is a collective index containing the indices $n_{e_k}, j_{e_k}, s_{e_k}$ for the electron and the indices n_{h_k}, j_{h_k} for the hole, respectively. For simplicity, in this work, we constrain ourselves to the case of one electron and one hole (one exciton), and the case of two electrons and two holes (two excitons). Without loss of generality, the electrons and holes locate in the upper and lower layers, respectively. Considering that the two conduction bands with different spins are close, here the electron state is associated with the spin index. In the second quantization, the many-body Hamiltonian is given by

$$H = \sum_{s,n,j} E^e_{j,n,s}c^\dagger_{j,n,s}c_{j,n,s} + \sum_{n,j} E^h_{j,n}d^\dagger_{j,n}d_{j,n} + H_{ee} + H_{hh} + H_{eh}, \tag{13}$$

$$H_{ee} = \frac{1}{2}\sum_{s,s'}\sum_{n_1,\dots,n_4}\sum_{j_1,\dots,j_4} V^{(ee)n_1,n_2,n_3,n_4}_{j_1,j_2,j_3,j_4} \times c^\dagger_{j_1,n_1,s}c^\dagger_{j_2,n_2,s'}c_{j_3,n_3,s'}c_{j_4,n_4,s}, \tag{14}$$

$$H_{hh} = \frac{1}{2}\sum_{n_1,\dots,n_4}\sum_{j_1,\dots,j_4} V^{(hh)n_1,n_2,n_3,n_4}_{j_1,j_2,j_3,j_4} \times d^\dagger_{j_1,n_1}d^\dagger_{j_2,n_2}d_{j_3,n_3}d_{j_4,n_4}, \tag{15}$$

$$H_{eh} = -\sum_{s}\sum_{n_1,\dots,n_4}\sum_{j_1,\dots,j_4} V^{(eh)n_1,n_2,n_3,n_4}_{j_1,j_2,j_3,j_4} \times c^\dagger_{j_1,n_1,s}d^\dagger_{j_2,n_2}d_{j_3,n_3}c_{j_4,n_4,s}, \tag{16}$$

where $c_{j,n,s}$ and $c^\dagger_{j,n,s}$ are the annihilation and creation operators for an electron with spin s, principal quantum number n, and angular momentum j, $E^e_{j,n,s}$ is the noninteracting energy of the electron state, $d_{j,n}$ and $d^\dagger_{j,n}$ are the operators for the hole, and $E^h_{j,n}$ is the energy of a hole state. H_{ee}, H_{hh}, and H_{eh} are the electron-electron, hole-hole, and electron-hole Coulomb interaction, respectively, where the Coulomb interaction matrix elements $V^{(ee)n_1,n_2,n_3,n_4}_{j_1,j_2,j_3,j_4}$, $V^{(hh)n_1,n_2,n_3,n_4}_{j_1,j_2,j_3,j_4}$, and $V^{(eh)n_1,n_2,n_3,n_4}_{j_1,j_2,j_3,j_4}$ are given in Appendix C in detail.

If there is only one electron and one hole in the system, then the Hamiltonian in Eq. (13) should exclude H_{ee} and H_{hh}. In our numerical calculation, we adopt the ED scheme

TABLE I. The parameters of two materials MoS_2 and WS_2, including lattice constants a, effective hopping integrals t, band gaps Δ, and SOC constant λ, are typically obtained through fitting first-principles band structure calculations. Note that here the conduction band of WS_2 is not relevant. The units are nm for length and eV for energy.

Material	a	Δ	t_e	t_h	λ
MoS_2	0.3193	1.66	1.1	1.1	0.075
WS_2	0.3197	1.79		1.37	0.23

mentioned above to solve the many-body Hamiltonian in Eq. (13). Then the energy spectra, electron-hole separation, pseudospin textures, and light absorption of the excitons can be studied. Considering the numerical complexity, we set an energy truncation of 50 meV for electron or hole states in QDs with radii 20 and 30 nm, when constructing the Hilbert space of the many-body states. For the radius of the QD being 10 nm (in the two-exciton case, we consider smaller QDs for saving computations), the truncation is increased to 100 meV.

III. RESULTS ON A SINGLE EXCITON

We conducted numerical studies on TMD van der Waals (vdW) heterostructures. Although there are numerous interesting 2D TMD materials [60,61], such as $MoTe_2$, with electronic and structural phase transitions, and bulk ReS_2, behaving as decoupled monolayers [62,63], here we specifically examine the exemplary MoS_2/MoS_2 double QDs and MoS_2/WS_2 double QDs. This choice is based on the suitability of the model, as well as the consideration of the layer-specific effective masses. Specifically, in a MoS_2/MoS_2 double-layer system, both the electron and hole are confined within the MoS_2 layer, characterized by conduction and valence band effective masses of approximately $0.7m_0$. In contrast, for a MoS_2/WS_2 double-layer system, the electron resides in the MoS_2 layer, while the hole locates in the WS_2 layer, with the ratio of effective mass of an electron in MoS_2 to that of a hole in WS_2 estimated at about 0.7/0.5 [7,64]. The TMDs family is vast and many members can be described using similar Hamiltonians.

Other systems could be analyzed in the same method, potentially yielding similar results. The parameters for MoS_2 and WS_2 used in numerical calculations are listed in Table I [6]. For simplicity, we consistently consider the electron and hole within a single valley throughout our analysis, which is deemed justifiable as the intervalley interaction is negligible due to the large kinetic difference between the two valleys. Additionally, achieving valley polarization through optical techniques is feasible in practice [48,49]. We further restrict the hole states with spin up and consider the electron states of spin up and spin down separately in the conduction band. It is motivated by the observation of a large splitting at the valence band edge due to sublattice pseudo-SOC.

A. Single-particle energy spectra in TMD QDs

The low-lying energy levels of single-particle states in TMD QDs with the magnetic field dependence are shown in Fig. 1. The energies with and without a magnetic field are calculated separately by using different formulas in Secs. II A and II B, respectively. One can see that the energy transition is smooth at the zero magnetic field limit, indicating that our analytical solutions for the eigenvalues with and without magnetic field match. These energy spectra are discrete, which is a direct consequence of finite-size confinement, compared to the bulk energy bands. Unlike a conventional semiconductor QD [29,65], the ground state of the conduction band is not degenerate at zero magnetic field; two spin states have a gap of ~0.1 meV due to the spin-sublattice coupling. As the magnetic field increases, the two spins states are further separated; the gap is about 0.6 meV up to 30 T. Similar phenomena have also been observed in earlier studies [65]. Eventually, Landau levels form with escalating magnetic field intensities. Notably, the spin splitting for hole states is much more significant, i.e., about 75 meV for MoS_2 and 215 meV for WS_2. This motivated our decision to use electronic states with two spins and spin-up hole states as the basis for constructing the Hilbert space in ED.

B. Interlayer exciton energy spectra

After characterizing the single-particle states in TMD QDs, we proceed to extend our investigation to two-particle systems, namely, electron-hole pairs within double-layer QDs. For accurate numerical calculations of quantum systems affected by Coulomb interactions, it is crucial to choose an appropriate set of eigenstates as the basis. The radii of the QDs in the electron and hole layers are the same, $R_e = R_h = 20$ nm. The radius is selected to manage the computational complexity. In Figs. 2 and 3, we illustrate the dependency of interlayer exciton energy on the magnetic field with varying interlayer distances. In Fig. 2, we can clearly observe that Coulomb interactions reduce the energy of excitons, and this reduction diminishes with the increase in interlayer separation since the Coulomb interaction is softened by the interlayer distance. Moreover, with the increase of the magnetic field, the single exciton still illustrates the Landau-type levels. It implies that quantum Hall effects may occur in these bosonic systems. In fact, the related phenomenon has been observed experimentally in a bilayer TMD system [66]. The Landau-level gaps in large magnetic fields are suppressed by the electron-hole Coulomb interaction, but will be recovered to the values of the noninteracting case when the separation of the two layers approaches infinity. Notably, the Landau-level gaps seem not to be increased monotonically with the increase of the distance d between the two layers. As shown in Fig. 1, the first Landau-level gap with $d = 5$ nm is obviously larger than that with $d = 10$ nm. However, when d increases to 15 nm, this gap increases and is more like the noninteracting case.

In Fig. 3, we extend our analysis to a MoS_2/WS_2 heterostructure, following the same context as depicted in Fig. 2. These results collectively illustrate the dependency of interlayer exciton energy on the magnetic field across distinct material systems. We observe that the energy of the low-lying excitonic states formed in the MoS_2/WS_2 heterostructure is lower than that in the MoS_2/MoS_2 heterostructure. This is attributed to the band mismatch between the conduction and valence bands while different materials are stacked. It leads to

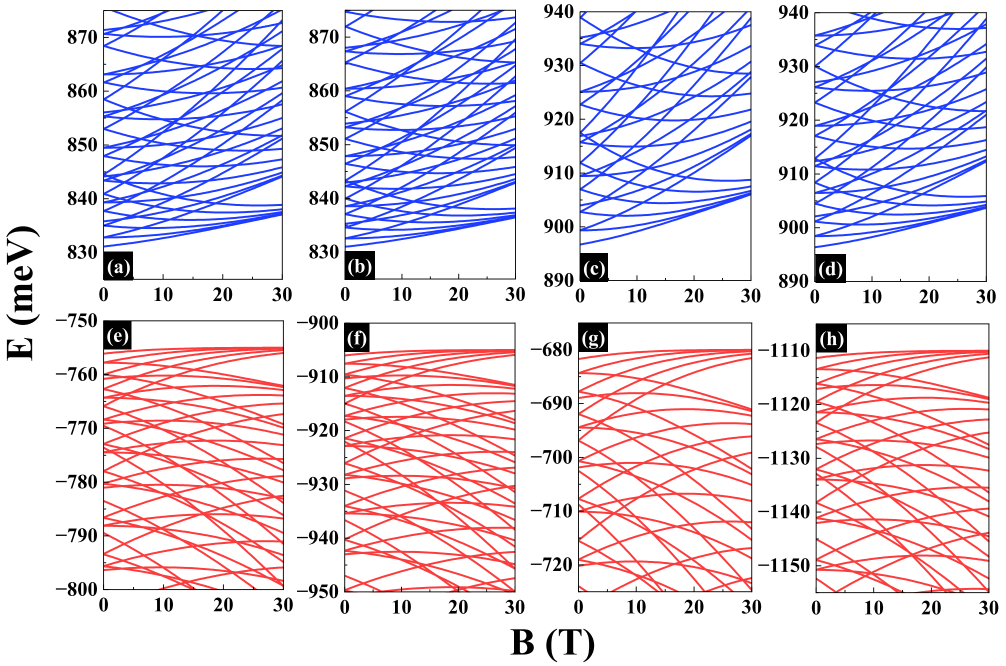

FIG. 1. The low-lying energy spectra of a single electron and a single hole in TMD QDs with radius $R = 20$ nm vary with perpendicular magnetic fields. For simplicity, only the first five levels of a principal quantum number are displayed. The energy spectra are provided for different TMDs with different spins: (a) MoS_2, conduction band with spin $s = 1$; (b) MoS_2, conduction band with $s = -1$; (c) WS_2, conduction band with $s = 1$; (d) WS_2, conduction band with $s = -1$; (e) MoS_2, valence band with $s = 1$; (f) MoS_2, valence band with $s = -1$ which is much farther away from the Fermi surface; (g) WS_2, valence band with $s = 1$; and (h) WS_2, valence band with $s = -1$. The electron and hole states are, respectively, indicated in blue and red.

the formation of a type-II band alignment [9] where the hole is confined in a WS_2 QD with lower single-particle energy. The Landau-type levels behavior of excitons in a magnetic field exhibits characteristics similar to that in the $\mathrm{MoS}_2/\mathrm{WS}_2$ double-layer QDs.

The ground-state energy of the interlayer exciton as a function of distance is shown in Fig. 4 for a $\mathrm{MoS}_2/\mathrm{MoS}_2$ and $\mathrm{MoS}_2/\mathrm{WS}_2$ double-layer QD. As shown in Figs. 4(a) and 4(b), it is apparent that the excitonic energy profile contains an initial augmentation followed by a slowly varied function

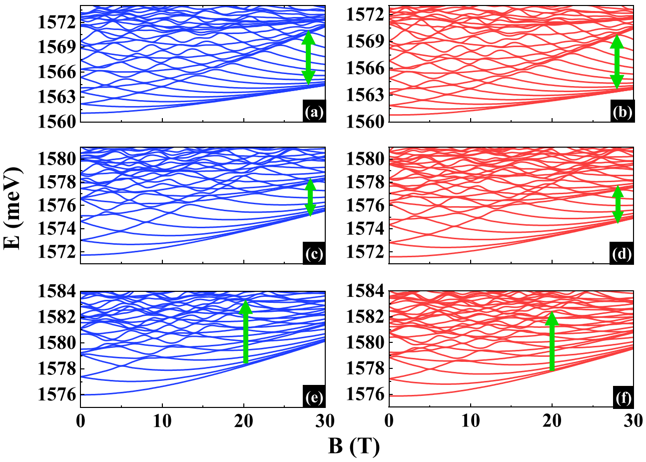

FIG. 2. The dependence of low-lying energy spectra of interlayer excitons on the magnetic field, where the electron and hole are confined within $\mathrm{MoS}_2/\mathrm{MoS}_2$ double-layer QDs with a radius of 20 nm. The left panels represent the excitons containing a spin-up electron, while the right panels are for spin down, indicating distinct spin arrangements. (a), (b) The interlayer exciton energy spectra with a 5 nm interlayer distance. (c), (d) The exciton spectra at a 10 nm interlayer distance. (e), (f) The exciton spectra at a 15 nm distance.

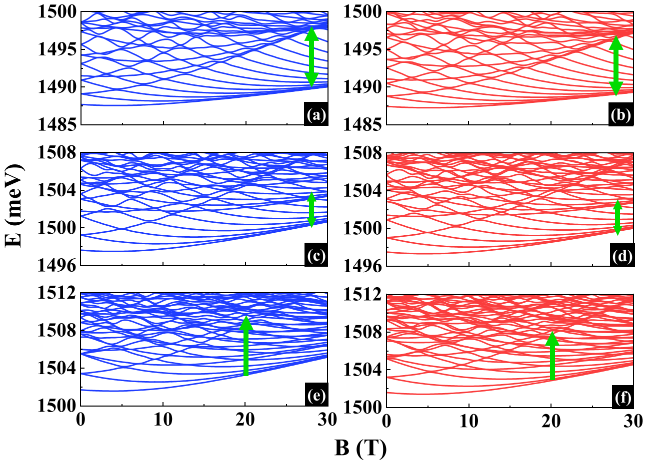

FIG. 3. Similar to Fig. 2, the dependence of low-lying energy spectra of interlayer excitons on the magnetic field, where the electron and hole are confined within $\mathrm{MoS}_2/\mathrm{WS}_2$ double-layer QDs with radius of 20 nm, respectively. The left and right panels represent the excitons containing electrons with spin up and spin down, respectively. (a), (b) The interlayer exciton energy spectra with a 5 nm interlayer distance. (c), (d) A 10 nm interlayer distance. (e), (f) A 15 nm distance.

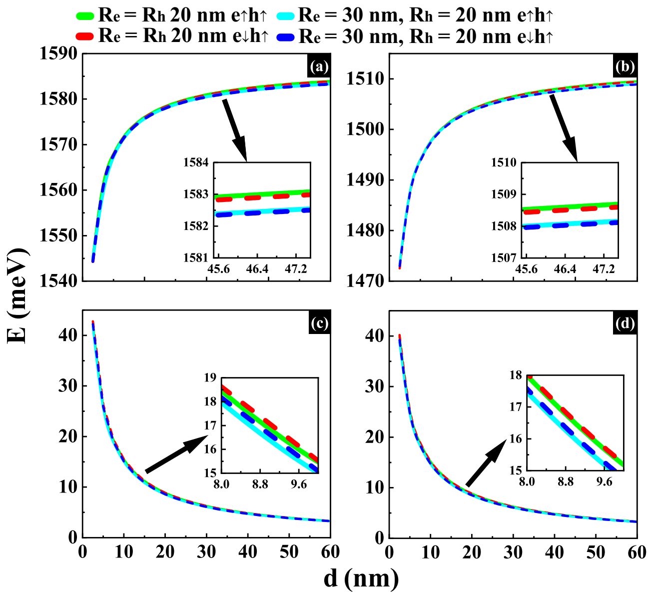

FIG. 4. The ground-state and binding energies of the interlayer excitons vary with the interlayer distance in the absence of a magnetic field: (a) Ground-state energy of MoS_2/MoS_2 double-layer QDs; (b) ground-state energy of MoS_2/WS_2 double-layer QDs, (c) binding energy of MoS_2/MoS_2 double-layer QDs, and (d) binding energy of MoS_2/WS_2 double-layer QDs. The solid line represents the energy for an exciton with an upward-spin electron, while the dashed line corresponds to a downward-spin electron. Both equal and unequal radius configurations are illustrated. The inset panels provide a detailed zoom-in of the energies.

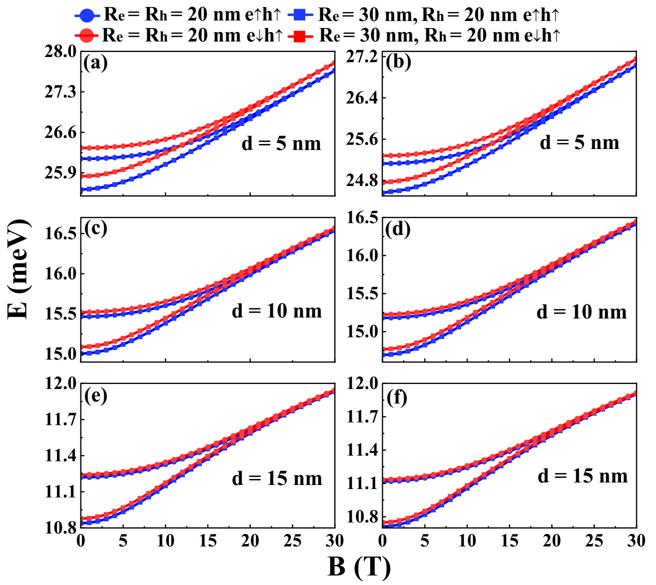

FIG. 5. Magnetic field dependence of binding energy of interlayer exciton ground state. The left panels are for MoS_2/MoS_2 double-layer QDs, while the right panels show results for MoS_2/WS_2 double-layer QDs. The interlayer distances are (a), (b) $d = 5$ nm, (c), (d) $d = 10$ nm, and (e), (f) $d = 15$ nm. Different electron spin configurations in the excitons are indicated by distinct colors, where blue and red denote the exciton with electron spin up and spin down, respectively. Circle symbol represents that two QDs have the same radius $R_e = R_h = 20$ nm, while the square symbol indicates $R_e = 30, R_h = 20$ nm.

of the interlayer separation. Consequently, from Figs. 4(c) and 4(d), there is a stronger bound energy at smaller interlayer distances. Nevertheless, the long-range nature of Coulomb forces [20] remains influential at a larger distance. In comparison, we also show the results where the radii of the double QDs differ, with the electron located in a 30-nm-radius dot and the hole in a 20-nm-radius dot. Both the exciton ground-state energy and binding energy slightly decrease compared to QDs with uniform radii. This reduction occurs because of the electron confined in larger QDs.

More results are presented in Fig. 5, showing the exciton binding energy as a function of the magnetic field. The binding energies all increase with the magnetic fields, which is attributed to the increase of the cyclotron motion, and decrease as the interlayer distance grows. Another notable feature is that excitons with spin-up electrons have lower binding energies than those with spin-down electrons. It is attributed to the different wave functions for different spins induced by the spin-valley coupling.

We also investigate a double-layer QD stacked with different radii, the upper QD providing an electron with radius 30 nm and the lower QD containing a hole with radius 20 nm. In this case, as shown in Fig. 5, the binding energies in weak magnetic fields are much lower than those in the double-layer QDs with identical radius of 20 nm. The single-particle density of states in larger QDs is higher and the noninteracting energy decreases more significantly than the Coulomb interaction, although the Coulomb interaction is also decreased by involving more single-particle states. When the magnetic field is strong, the single-particle states approach degeneracy in Landau levels, causing the binding energies for QDs of different sizes to converge.

C. Electron-hole separation

The Coulomb interaction spatially constrains the electrons and holes, differing from intralayer excitons. In the xOy plane, the electron-hole separation is expressed as

$$\langle \mathbf{r}_e - \mathbf{r}_h \rangle = \sum_{i,k} C_i^* C_k \langle i_e; i_h | \mathbf{r}_e - \mathbf{r}_h | k_e; k_h \rangle. \tag{17}$$

Here, C_i and C_k represent the expansion coefficients of the ground state of the exciton obtained by diagonalizing the Hamiltonian, $|\mathrm{GS}\rangle = \sum_i C_i |i_e; i_h\rangle$. This measure provides insight into the spatial distribution and binding nature of the exciton.

In Fig. 6, we show the electron-hole separation as a function of magnetic fields in the MoS_2/WS_2 double-layer QDs only. For the MoS_2/MoS_2 heterostructure case, the electron is generally located exactly upon the hole, and the separation $\langle \mathbf{r}_e - \mathbf{r}_h \rangle$ approaches zero (up to ∼0.06 nm). Comparing Fig. 6(a) with 6(b), and Fig. 6(c) with 6(d), the separation of excitons with different spin electrons is minimal. Figures 6(a) and 6(b) show results with identical radius 20 nm of the electron and hole layers, indicating that the separation magnitude is much smaller than the system's size. In contrast, as shown in Figs. 6(c) and 6(d), the separation of the system with

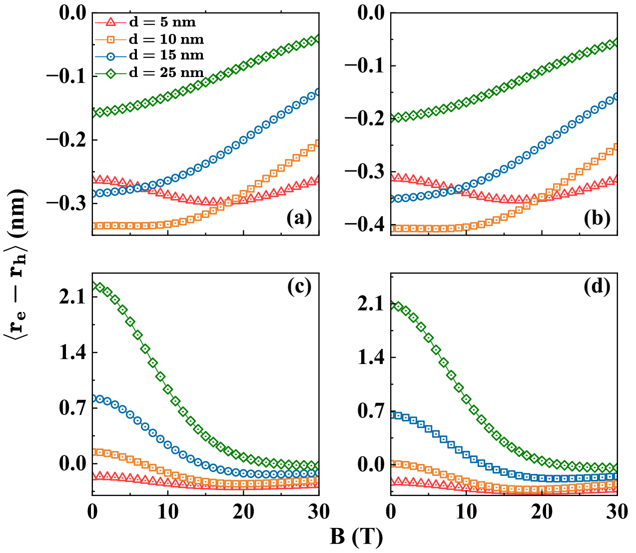

FIG. 6. Evolution of the ground-state electron-hole separation $\langle \mathbf{r}_e - \mathbf{r}_h \rangle$ with magnetic fields in different distances for the MoS_2/WS_2 heterostructure. The top panels show separations in QDs with identical 20 nm radius, while the bottom panels show separations in QDs with $R_e = 30$ nm in the electron layer and $R_h = 20$ nm in the hole layer. The interlayer exciton separation for different electron spin: (a), (c) electron spin up; (b), (d) electron spin down.

$R_e = 30$ nm and $R_h = 20$ nm varies significantly with magnetic field. In weak magnetic field, the separation is one magnitude larger than the case of identical radius since the orbit of a low-energy single-particle wave function is different. In large magnetic field, due to the Landau quantization, the difference of separation between the two cases is not obvious.

Notably, unlike the energy of the ground state, the absolute value of separation $|\langle \mathbf{r}_e - \mathbf{r}_h \rangle|$ does not vary monotonously with either the magnetic field or the distance between the two layers. With increase of distance, the separation starts to increase and then decreases, in the case of identical radius of two QDs. However, the situation is reversed in the case of different radii of two QDs. As the magnetic field varies, the change of the $|\langle \mathbf{r}_e - \mathbf{r}_h \rangle|$ becomes even more complicated. Comparing to the excitons in conventional semiconductor QDs, the anomalous change of electron-hole separation as well as the density shape of the exciton here is attributed to the complex orbit of the wave function induced by SOC in the system, which may be observed by detecting the wave function's orbitals [67].

D. Pseudospin textures of interlayer excitons

Topological textures of spin fields in QDs are induced by SOC, which also plays an important role in TMDs. Studying topological features in QDs boosts spintronics by refining spin control and enhances quantum information processing by improving qubit storage and manipulation [68]. Similar to spin, the two sublattices of TMDs can be represented by pseudospin. In the Hamiltonian of TMD QDs, the pseudospin-orbit coupling, similar to Rashba and Dresselhaus SOC, also results in a nontrivial pseudospin texture. The pseudospin fields for electron and hole in an exciton can be defined as follows:

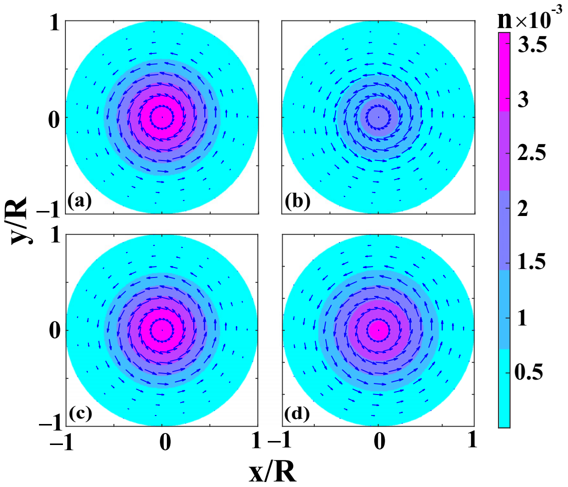

FIG. 7. Ground-state pseudospin fields $(\sigma_x^\alpha, \sigma_y^\alpha)$ of interlayer excitons with electron and hole spin-up at magnetic field $B = 1$ T. (a) and (c) The pseudospin textures of the electron and the hole in interlayer exciton in MoS_2/MoS_2 double-layer QDs with radii $R_e = R_h = 20$nm, respectively. The distance between the two layers is 5 nm. (b) and (d) The pseudospin textures of the electron and the hole in interlayer exciton in MoS_2/WS_2 double-layer QDs with $R_h = 20$nm and $R_e = 30$nm. The distance between the two layers is 10 nm.

$$\sigma^\alpha_{x,y}(\mathbf{r}) = \sum_{i,k} C_i^* C_k \delta_{i_{\bar\alpha},k_{\bar\alpha}} \left(\chi^{\alpha*}_{2i}\chi^\alpha_{1k} \pm \chi^{\alpha*}_{1i}\chi^\alpha_{2k}\right) \times \exp\left[i\theta\left(\pm\tau + j_{k_\alpha} - j_{i_\alpha}\right)\right], \tag{18}$$

and the density is given by

$$n^\alpha(\mathbf{r}) = \sum_{i,k} C_i^* C_k \delta_{i_{\bar\alpha},k_{\bar\alpha}} \left(\chi^{\alpha*}_{1i}\chi^\alpha_{1k} + \chi^{\alpha*}_{2i}\chi^\alpha_{2k}\right) \times \exp\left[i\left(j_{k_\alpha} - j_{i_\alpha}\right)\theta\right], \tag{19}$$

where α denotes the electron or hole, $\bar\alpha$ denotes the hole or electron, respectively, and χ^α correspond to two components in the spinor wave function of a state. The in-plane pseudospin field is represented by $\phi^\alpha(\mathbf{r}_\alpha) = (\sigma_x^\alpha, \sigma_y^\alpha)$. A winding number Q describes the topological property of the textures of the in-plane (pseudo)spin fields in real space and is defined as [68]

$$Q = \frac{1}{2\pi}\oint d\phi = \frac{1}{2\pi}\oint \frac{\sigma_x(\mathbf{r})d\sigma_y(\mathbf{r}) - \sigma_y(\mathbf{r})d\sigma_x(\mathbf{r})}{\sigma_x(\mathbf{r})^2 + \sigma_y(\mathbf{r})^2}.$$

In Fig. 7, two examples of the pseudospin fields of the ground states are displayed. The pseudospins of the electron and hole are textured with nontrivial topological charge $Q = 1$ [69]. The topological spin fields in QDs induced by Rashba or Dresselhaus SOC usually have zero vorticity, while both topological charge and vorticity are nonzero here since the exciton is in the K valley with $\tau = 1$. We note that in the K' valley, the pseudospin textures are more like those with Dresselhaus SOC given that $\tau = -1$. The pseudospin textures of the first excited state of the exciton are shown in Fig. 8. Similar to the QD with Rashba or Dresselhaus SOC,

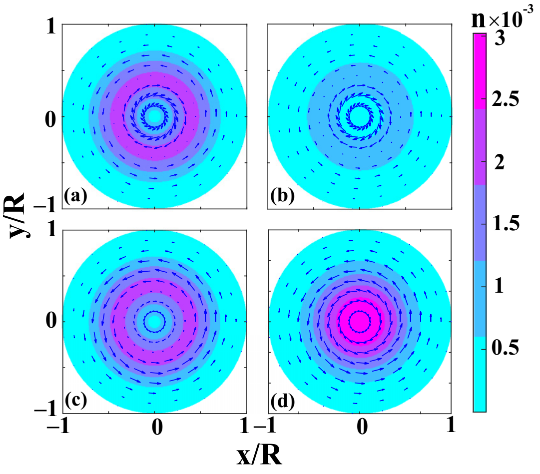

FIG. 8. The same as Fig. 7, but depicting the pseudospin texture for the first excited state under a magnetic field of $B = 5$ T.

the topological charge of the pseudospin remains unchanged, but its vorticity is inverse.

E. Light absorption

Far-infrared (FIR) magneto-optical absorption spectroscopy is a technique used to study and utilize the optical properties of materials. In QDs, the optical selection rules are primarily governed by spatial confinement and the system's geometric characteristics. The confinement of the QD converts the energy bands into discrete energy levels akin to atomic systems, i.e., making QDs the artificial atoms [70]. This pronounced confinement effect, raising angular momenta of J_{tot}, governs their optical properties with unique light-matter interaction behaviors [45,46,48,49]. The radius of the QD discussed here is typically only tens of nanometers, i.e., significantly smaller than the wavelength of far-infrared light corresponding to the energy gaps of the system, if only the transitions between the exciton levels are considered. Therefore, we can compute the exciton light absorption using the dipole approximation [71–73]. The incident light is supposed to be perpendicular to the plane of TMDs. The dipole transition matrix element from state $|k\rangle$ to state $|i\rangle$ is denoted as $D_{ik} = \langle i|\boldsymbol{\varepsilon} \cdot \boldsymbol{r}|k\rangle$, where $\boldsymbol{\varepsilon}$ represents the polarization vector lying in the xOy plane. The dipole transition matrix element depends on the polarization of the incident light. Generally, we consider the incident light to be unpolarized. For a single particle in QDs, the dipole transition matrix element is given by

$$D_{ik} = \pi(\Omega_x + i\Omega_y)\int r^2 dr(\chi_{1i}^*\chi_{1k} + \chi_{2i}^*\chi_{2i}), \tag{20}$$

where $\Omega_{x,y} = \delta_{m_k+1,m_i} \pm \delta_{m_k-1,m_i}$, m is the orbital angular momentum quantum number, and χ_{12} is spinor corresponds to two sublattices.

According to the transition selection rule, only transitions with $\Delta m = m_i - m_k = \pm 1$ are allowed between the initial state $|i\rangle$ and final state $|k\rangle$. Note that this selection rule is only valid for the intra-exciton transitions between the exciton states. The transition between an exciton state and the vacuum, as the exciton recombination discussed in Ref. [74], is not considered here. We calculate the amplitude of the dipole transition matrix element as $A_{k\to i} = \sum_{i,k} C_i^* C_k \langle i_e, i_h|\mathbf{r}_h - \mathbf{r}_e|k_e, k_h\rangle$. The intensity of absorption is proportional to $|A_{k\to i}|^2$. We consider only the transition from ground state to excited state.

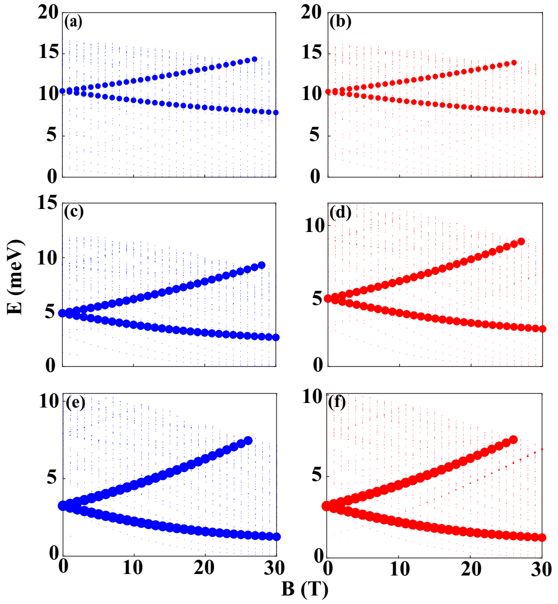

FIG. 9. Dipole-allowed optical absorption spectra of MoS$_2$/MoS$_2$ double-layer QDs for various interlayer distances. The left panels show the results with electron spin up, while the right panels illustrate for spin down. (a), (b) Results with interlayer distance of $d = 5$ nm, (c), (d) for an interlayer distance of $d = 10$ nm, and (e), (f) for $d = 15$ nm. The radii of the QDs in both layers are 20 nm. The size of the points is proportional to the intensity of the light absorption.

Figure 9 illustrates the dipole-allowed light absorption of interlayer excitons across different interlayer distances under varying magnetic fields. Without interactions, some transition modes are allowed by the selection rules, but Coulomb interactions make them forbidden. Comparing cases with different interlayer distances, we notice that dipole-allowed transitions in systems with smaller interlayer distances favor modes with higher energy. The intensity of the transition modes increases with larger interlayer distances. Moreover, Fig. 10 shows dipole-allowed optical absorption spectra of a MoS$_2$/MoS$_2$ heterostructure for QDs with radii $R_e = 30$ nm and $R_h = 20$ nm. We find that light absorption varies with interlayer distance similarly to Fig. 9, but more transition modes are available.

IV. RESULTS ON BIEXCITON

We have discussed the physical quantities of a single interlayer exciton in the previous section. It is worthwhile to explore the case of interacting interlayer excitons, which is described by the full many-body Hamiltonian in Eq. (13). For simplicity, here we consider a biexciton system containing two electrons and two holes. The electrons and holes still locate in the upper and lower layers, respectively. The Hamiltonian contains intralayer electron-electron and

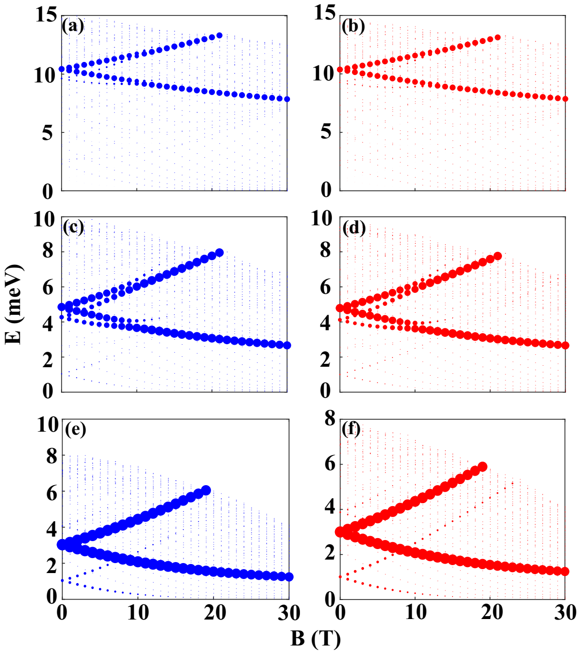

FIG. 10. The same dipole-allowed optical absorption spectra as Fig. 9, but the radii of the electron and hole layer are $R_e = 30$ nm and $R_h = 20$ nm, respectively.

hole-hole interactions compared to that of a single exciton system. We discuss two scenarios, where electrons either have identical or opposite spins, and the spin of the holes is fixed. The biexciton system exhibits more complex interactions than the single exciton system, resulting in different features.

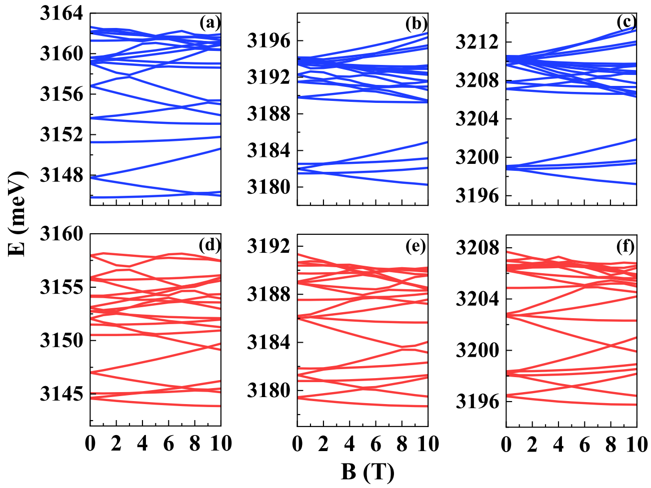

FIG. 11. The dependence of low-lying energy spectra of biexcitons on the magnetic field, where the electrons and holes are confined within MoS_2/MoS_2 double-layer QDs with the same radius of 10 nm. (a)–(c) The system containing two electrons with the same spin; (d)–(f) two electrons with different spins. (a)–(c) The energy spectra with interlayer distances 5, 10, and 15 nm, respectively. (d)–(f) The same distance as (a)–(c), respectively.

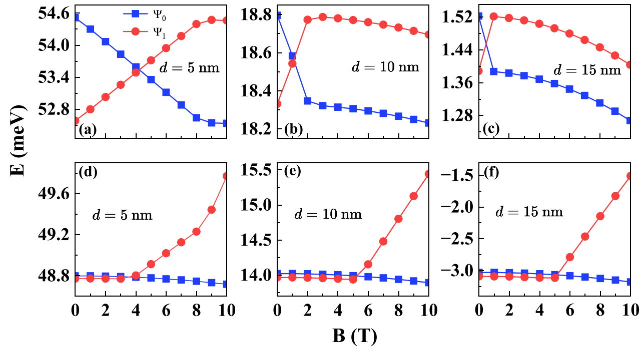

FIG. 12. Magnetic field dependence of the binding energy of a biexciton ground state and the first excited state. (a)–(f) correspond to the cases in Figs. 11(a)–11(f), respectively. (a)–(c) The biexciton containing two electrons with spin up; (d)–(f) two electrons with different spins.

Again, by employing the ED, the energy spectra are shown in Fig. 11, indicating rich energy-level structures due to many-body correlations. As the interlayer distance increases, the ground state and low-lying excited states exhibit higher energy. Remarkably, the four low-lying states are well gapped from higher states with sufficiently large interlayer distance when the two electrons have the same spin, as shown in Figs. 11(b) and 11(c). By comparing the energy spectra in Figs. 11(a)–11(c) and Figs. 11(d)–11(f), when the electrons have different spins, we find that some levels emerge. Particularly, the new ground state with twofold degeneracy at zero magnetic field due to the Kramers pair appears, and its energy is significantly suppressed by the exchange interaction between two different spins. Moreover, the gap between low-lying levels and higher levels becomes not obvious; it only exists in weak magnetic fields, as shown in Figs. 11(e) and 11(f). For more information, the binding energies of the ground state and the first excited state are displayed in Fig. 12. The mutations in binding energies arises from the transition of the ground state with an increase of the magnetic field.

The dipole-allowed light absorptions of biexciton systems across different interlayer distances under varying magnetic fields are shown in Fig. 13. Compared to the case of a single interlayer exciton, more absorption modes are visible. The

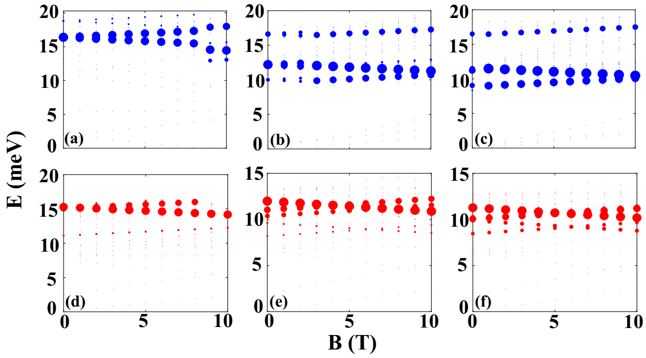

FIG. 13. Dipole-allowed optical absorption spectra of a biexciton for various interlayer distances. (a)–(c) The biexciton containing two electrons with spin up; (d)–(f) two electrons with different spin. (a), (d) Results with interlayer distance of $d = 5$ nm; (b), (e) interlayer distance of $d = 10$ nm; and (c), (f) $d = 15$ nm. The radii of the QDs in both layers are 10 nm.

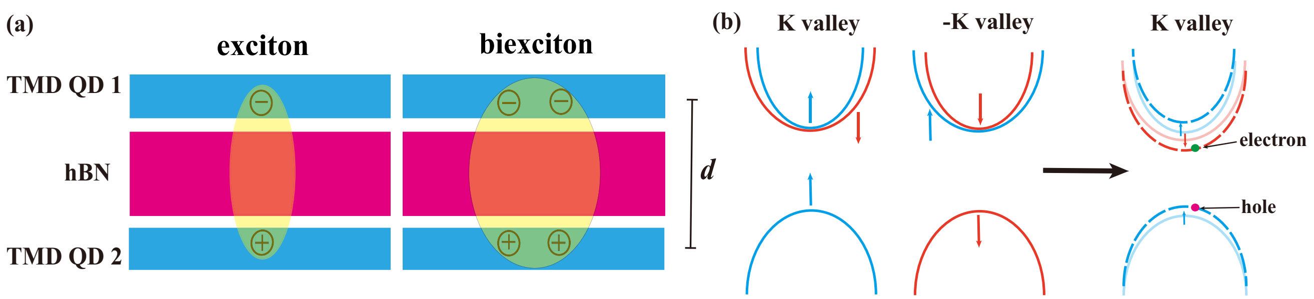

FIG. 14. The schematic double-layer system and band structure of TMDs near the Fermi surface. (a) An electron confined in a TMD layer and a hole in the other TMD layer. (b) The lower bands in the valence band are neglected since they are far away from the Fermi surface. Only one valley, say, valley K, is considered. The right panel indicates the bands (dashed lines) shift by Zeeman coupling in a magnetic field [43]. Electrons and holes are marked in different bands, as well as in different layers.

mutation of the absorption intensity is attributed to the transition of the ground state when the two electrons have the same spin. For the case that two electrons have different spins, no transition occurs in the ground state. The level crossing in higher levels does not significantly influence the absorption. Consequently, by measuring the light absorption spectra, one can distinguish the electron spins in the biexciton systems.

It is noted that only biexcitons in MoS_2/MoS_2 double-layer QDs are studied here. The energy spectra and light absorptions should remain qualitatively unchanged in MoS_2/WS_2 double-layer QDs, as the physical properties of a single exciton (with the exception of the electron-hole separation) are not significantly altered by the transition from MoS_2/MoS_2 double-layer QDs to MoS_2/WS_2 double-layer QDs.

V. SUMMARY

We constructed a double-layer TMD QDs model with adjustable interlayer distance based on analyzing a single particle in a hard-wall potential TMD QD subjected to an external magnetic field. Impurities and edge deformations may affect the transport properties [72,75], but their impact is expected to be minimal if the quantum dots studied in this work are well constructed. If the edge of the QD is only slightly deformed, our results remain unchanged qualitatively. This nanostructure enables the formation of interlayer excitons, which can be achieved through the modulation of band energies via external voltage or by leveraging the intrinsic properties of TMDs, and represent one or more interlayer excitons with electron-electron, hole-hole, and electron-hole correlations. By employing ED, we numerically explore this interlayer system with Coulomb interaction. We report on several characteristics of an interlayer exciton, including energy spectrum, binding energy, spatial distribution of electron and hole topological pseudospin textures, and optical absorption spectrum with external magnetic fields in adjustable interlayer distances. Remarkably, the Landau-level gap, i.e., the electron-hole separation in an exciton, varies nonmonotonously with the increase of the interlayer distance due to the sublattice pseudo-spin-orbit coupling in TMDs. Moreover, the ground state and excitation states of the interlayer exciton are all pseudospin textured topologically by this pseudo-spin-orbit coupling.

Furthermore, we studied many-body systems with two interacting interlayer excitons which contain two electrons and two holes. The energy spectra and light absorptions are also numerically calculated. Our numerical calculations show energy spectra with interaction-driven spectral splitting and enhanced binding energies. The optical absorption shifts under magnetic fields emerge, which are not observed in simpler systems. These findings highlight the tunable potential of TMD QDs for advanced quantum and optoelectronic technologies, allowing precise control of excitonic properties through external fields and structural tuning. Our detailed analysis of their response to magnetic fields and interlayer distance fills in gaps in knowledge about the mechanism of formation and possible consequences within the nanoelectronics and quantum computing research domains.

ACKNOWLEDGMENTS

This work was supported by the National Natural Science Foundation of China under Grant No. 11804396. The authors acknowledge Xiaoming Yuan, Chuanchun Shu, Yutao Hu, and Yi Jiang for helpful discussions. We are grateful to the High Performance Computing Center of Central South University for partial support of this work.

APPENDIX A: TMD DOUBLE LAYERS AND BAND STRUCTURE

The double-layer structure and band selection scenario is schematically illustrated in Fig. 14. The valley is supposed to be polarized. Electrons and holes are from different layers. Building on this framework, double TMD QDs can be engineered using gate control or nanoflakes.

APPENDIX B: DERIVATION OF BASIS

In this Appendix, we derive the eigenstates of the TMD QD, which are utilized as the basis for deriving the matrix elements in our numerical calculations. The derivation begins with the general form of the TMD QD Hamiltonian, as detailed in Eq. (2),

$$H = \begin{pmatrix} \frac{\Delta}{2} & \frac{at}{\hbar}[\tau(p_x + eA_x) - i(p_y + eA_y)] \\ \frac{at}{\hbar}[\tau(p_x + eA_x) + i(p_y + eA_y)] & -\frac{\Delta}{2} + \lambda\tau s \end{pmatrix} + V(r)\begin{pmatrix} 1 & 0 \\ 0 & -1 \end{pmatrix}. \tag{B1}$$

By using the symmetric gauge $\mathbf{A} = \frac{B}{2}(-y, x, 0)$, we can get

$$\frac{at}{\hbar}[\tau(p_x + eA_x) - i(p_y + eA_y)] = -iat\exp(-i\tau\theta)\left(\tau\frac{\partial}{\partial r} - i\frac{1}{r}\frac{\partial}{\partial\theta} + e\frac{B}{2\hbar}r\right), \tag{B2a}$$

$$\frac{at}{\hbar}[\tau(p_x + eA_x) + i(p_y + eA_y)] = -iat\exp(i\tau\theta)\left(\tau\frac{\partial}{\partial r} + i\frac{1}{r}\frac{\partial}{\partial\theta} - e\frac{B}{2\hbar}r\right). \tag{B2b}$$

Then the Hamiltonian of the TMD QD in the polar coordinates becomes

$$H = \begin{pmatrix} \frac{\Delta}{2} & -iat\exp(-i\tau\theta)\left(\tau\frac{\partial}{\partial r} - i\frac{1}{r}\frac{\partial}{\partial\theta} + e\frac{B}{2\hbar}r\right) \\ -iat\exp(i\tau\theta)\left(\tau\frac{\partial}{\partial r} + i\frac{1}{r}\frac{\partial}{\partial\theta} - e\frac{B}{2\hbar}r\right) & -\frac{\Delta}{2} + \lambda\tau s \end{pmatrix} + V(r)\sigma_z. \tag{B3}$$

1. Zero magnetic field

In the absence of a magnetic field, the Dirac equation can be reformulated into two coupled differential equations using the eigenstates defined in Eq. (4) and expressed in dimensionless units,

$$at\left[\tau\frac{\partial}{\partial r} + \frac{1}{r}\left(j + \frac{\tau}{2}\right)\right]\chi_2(r) = \left(E - \frac{\Delta}{2}\right)\chi_1(r), \tag{B4a}$$

$$at\left[\tau\frac{\partial}{\partial r} - \frac{1}{r}\left(j - \frac{\tau}{2}\right)\right]\chi_1(r) = -\left(E + \frac{\Delta}{2} - \lambda\tau s\right)\chi_2(r). \tag{B4b}$$

We can deduce that $\frac{[\tau\frac{\partial}{\partial\rho} + \frac{1}{\rho}(j + \frac{\tau}{2})]\chi_2(r)}{(\varepsilon - \frac{1}{2}\delta)} = \chi_1(r)$ and subsequently apply it to Eq. (B4a), and $\chi_2(\rho)$ yields the following differential equation:

$$\rho^2\frac{\partial}{\partial\rho^2}\chi_2(\rho) + \rho\frac{\partial}{\partial\rho}\chi_2(\rho) - \left(j + \frac{\tau}{2}\right)^2\chi_2(\rho) + \kappa^2\rho^2\chi_2(\rho) = 0. \tag{B5}$$

Equation (B5) is a Bessel differential equation, for which a specific solution is obtained. Following this, the solution is incorporated into Eq. (B4a) and, with the subsequent application of the Bessel function relations,

$$\frac{d}{dx}[x^v J_v(x)] = x^v J_{v-1}(x), \tag{B6a}$$

$$\frac{d}{dx}[x^{-v} J_v(x)] = -x^{-v} J_{v+1}(x). \tag{B6b}$$

The wave function is successfully derived,

$$\psi = N\begin{pmatrix} e^{i(j-\frac{\tau}{2})\theta}\frac{2at}{2E-\Delta}\sqrt{\kappa}\varrho J_{(j-\frac{\tau}{2})}(\sqrt{\kappa}r) \\ ie^{i(j+\frac{\tau}{2})\theta}\varrho J_{(j+\frac{\tau}{2})}(\sqrt{\kappa}r) \end{pmatrix}, \tag{B7}$$

where

$$\varrho = \begin{cases} 1, & j + \frac{\tau}{2} \geqslant 0 \\ (-1)^{j+\frac{\tau}{2}}, & j + \frac{\tau}{2} < 0. \end{cases} \tag{B8}$$

2. Nonzero magnetic field

Continuing with the analysis of magnetic field flux within the QDs, we arrive at the following expressions:

$$at\left[\tau\frac{\partial}{\partial r} + \frac{1}{r}\left(j + \frac{\tau}{2}\right) + e\frac{B}{2\hbar}r\right]\chi_2(r) = \left(E - \frac{\Delta}{2}\right)\chi_1(r), \tag{B9a}$$

$$-at\left[\tau\frac{\partial}{\partial r} - \frac{1}{r}\left(j - \frac{\tau}{2}\right) - e\frac{B}{2\hbar}r\right]\chi_1(r) = \left[E - \left(-\frac{\Delta}{2} + \lambda\tau s\right)\right]\chi_2(r). \tag{B9b}$$

Adopting dimensionless units, we obtain

$$\left[\tau\frac{\partial}{\partial\rho} + \frac{1}{\rho}\left(j + \frac{\tau}{2}\right) + \beta\rho\right]\chi_2(\rho) = \left(\varepsilon - \frac{1}{2}\delta\right)\chi_1(\rho), \tag{B10a}$$

$$\left[\tau\frac{\partial}{\partial\rho} - \frac{1}{\rho}\left(j - \frac{\tau}{2}\right) - \beta\rho\right]\chi_1(\rho) = -\left(\varepsilon + \frac{1}{2}\delta - \Lambda\tau s\right)\chi_2(\rho), \tag{B10b}$$

and we get $-\frac{[\tau\frac{\partial}{\partial\rho} - \frac{1}{\rho}(j - \frac{\tau}{2}) - \beta\rho]\chi_1(\rho)}{\varepsilon + \frac{1}{2}\delta - \Lambda\tau s} = \chi_2(\rho)$ from Eq. (B10b); subsequently, that is substituted into Eq. (B10a), yielding

$$\frac{\partial}{\partial\rho^2}\chi_1(\rho) - \left(j - \frac{\tau}{2}\right)^2\frac{1}{\rho^2}\chi_1(\rho) + \frac{1}{\rho}\frac{\partial}{\partial\rho}\chi_1(\rho) - 2\left(j + \frac{\tau}{2}\right)\beta\chi_1(\rho) - \beta^2\rho^2\chi_1(\rho) + \left(\varepsilon + \frac{1}{2}\delta - \Lambda\tau s\right) \times \left(\varepsilon - \frac{1}{2}\delta\right)\chi_1(\rho) = 0. \tag{B11}$$

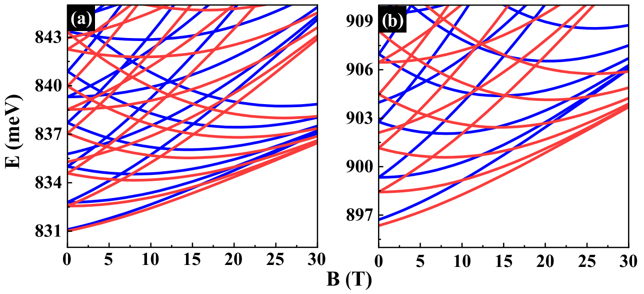

FIG. 15. This figure provides a zoomed-in view of the electron states from Fig. 1, illustrating the low-lying energy spectra of a single electron in TMD QDs with $R = 20$ nm. (a) $\mathrm{MoS_2}$ QD; (b) $\mathrm{WS_2}$ QD. Blue and red lines represent spin-up and spin-down states, respectively, plotted together for comparison.

We make the ansatz $\chi_1(\rho) = \rho^{|j-\frac{\tau}{2}|}\exp\left(-\frac{\beta\rho^2}{2}\right)\chi_0(\rho^2)$ and define $x = \beta\rho^2$, which enables us to derive

$$x\frac{\partial^2}{\partial x^2}\chi_0(x) + \left(\left|j-\frac{\tau}{2}\right| + 1 - x\right)\frac{\partial}{\partial x}\chi_0(x) - \left[\frac{1}{2}\left(j+\frac{\tau}{2}+\left|j-\frac{\tau}{2}\right|+1\right) - \frac{\left(\varepsilon+\frac{1}{2}\delta-\Lambda\tau s\right)\left(\varepsilon-\frac{1}{2}\delta\right)}{4\beta}\right]\chi_0(x) = 0, \tag{B12}$$

where we introduce the definitions $b = |j-\frac{\tau}{2}|+1$ and $\alpha = \frac{1}{2}(j+\frac{\tau}{2}+|j-\frac{\tau}{2}|+1) - \frac{(\varepsilon+\frac{1}{2}\delta-\Lambda\tau s)(\varepsilon-\frac{1}{2}\delta)}{4\beta}$. The resulting equation is identified as a confluent hypergeometric equation, from which the solution is deduced, $\chi_1(\rho) = C\rho^{|j-\frac{\tau}{2}|}\exp(-\frac{\beta\rho^2}{2})_1F_1(\alpha, b, \beta\rho^2)$. By incorporating another component into Eq. (B10b) and substituting it, we derive the wave function in the presence of a magnetic field,

$$\psi = N\begin{pmatrix} e^{i(j-\frac{\tau}{2})\theta}\rho^{|j-\frac{\tau}{2}|}\exp\left(-\frac{\beta\rho^2}{2}\right){}_1F_1(\alpha, b, \beta\rho^2) \\ ie^{i(j+\frac{\tau}{2})\theta}\rho^{|j-\frac{\tau}{2}|-1}\exp\left(-\frac{\beta\rho^2}{2}\right)\gamma\Gamma(\rho)\end{pmatrix}, \tag{B13}$$

where we define $\Gamma(\rho) = \xi_1F_1(\alpha, b, \beta\rho^2) + \tau\frac{2\alpha}{b}\beta\rho^2_1F_1(\alpha+1, b+1, \beta\rho^2)$ with $\xi = \tau|j-\frac{\tau}{2}| - j + \frac{\tau}{2} - (\tau+1)\beta\rho^2$ and $\gamma = -(\varepsilon+\frac{1}{2}\delta-\Lambda\tau s)^{-1}$.

3. Eigenvalues equations

Upon deriving the wave function, the energy quantization condition is obtained by applying the infinite-mass boundary condition at the quantum dot radius R. By numerically solving Eq. (8), the eigenvalue $E(\tau, n, j, s)$ is determined, where the negative energy corresponds to the hole states and the positive energy corresponds to the electron states. The resulting energy levels are presented in Fig. 1, with Fig. 15 offering a zoomed-in view. For the electron states, both spin orientations are plotted together for comparison.

APPENDIX C: COULOMB INTERACTION MATRIX ELEMENTS

The Hamiltonian of the many-exciton system is given by Eqs. (13)–(16). To numerically solve the many-body Hamiltonian, it is essential to first derive the matrix elements of the Coulomb interaction. The Coulomb potential between the electron and hole across different layers is given by $V_{eh} = \frac{-e^2}{\epsilon\sqrt{|\mathbf{r}_e-\mathbf{r}_h|^2+d^2}}$, with dielectric constant $\epsilon = 7.1$. The Coulomb interaction matrix elements are established by the field operators,

$$\Phi_e(\mathbf{r}_e) = \sum_{s,n,j}\psi_{j,n,K,s}(\mathbf{r}_e)c_{j,n,s}, \tag{C1}$$

$$\Phi_h(\mathbf{r}_h) = \sum_{n,j}\psi_{j,n,K,\downarrow}(\mathbf{r}_h)d_{j,n}, \tag{C2}$$

where we include the quantum numbers in the wave functions and operators, including angular momentum j, principal quantum number n, and electron spin index s. We froze the spin of the valence band to ↓ and suppose the valley is polarized to K. By defining

$$\Xi^{(e)j_k,n_k,\tau_k,s_k}_{j_i,n_i,\tau_i,s_i}(\mathbf{q}) = \int_0^{R_e} d\mathbf{r_e}\,\psi^*_{j_i,n_i,\tau_i,s_i}(\mathbf{r_e})\psi_{j_k,n_k,\tau_k,s_k}(\mathbf{r_e})e^{i\mathbf{q}\cdot\mathbf{r_e}},$$

$$\Xi^{(h)j_k,n_k,\tau_k,s_k}_{j_i,n_i,\tau_i,s_i}(\mathbf{q}) = \int_0^{R_h} d\mathbf{r_h}\,\psi^*_{j_i,n_i,\tau_i,s_i}(\mathbf{r_h})\psi_{j_k,n_k,\tau_k,s_k}(\mathbf{r_h})e^{i\mathbf{q}\cdot\mathbf{r_h}},$$

the interlayer electron-hole Coulomb interaction matrix element is

$$V^{(eh)n_1,n_2,n_3,n_4}_{j_1,j_2,j_3,j_4} = -\int qdqd\theta\frac{2\pi e^2}{\epsilon q}e^{-qd}\,\Xi^{(e)j_4,n_4,K,s}_{j_1,n_1,K,s}(\mathbf{q}) \times \Xi^{(h)j_3,n_3,K,\downarrow}_{j_2,n_2,K,\downarrow}(-\mathbf{q}), \tag{C3}$$

where d is the interlayer separation. For the intralayer Coulomb potential, $V_{ee} = \frac{e^2}{\epsilon\sqrt{|\mathbf{r}_{e_1}-\mathbf{r}_{e_2}|^2}}$, the Coulomb interaction matrix element with different spins in H_{ee} is

$$V^{(ee)n_1,n_2,n_3,n_4}_{j_1,j_2,j_3,j_4} = \int qdqd\theta\frac{2\pi e^2}{\epsilon q}\,\Xi^{(e)j_4,n_4,K,s}_{j_1,n_1,K,s}(\mathbf{q}) \times \Xi^{(h)j_3,n_3,K,s'}_{j_2,n_2,K,s'}(-\mathbf{q}), \tag{C4}$$

and the hole-hole interaction term in H_{hh} with the Coulomb potential, $V_{hh} = \frac{e^2}{\epsilon\sqrt{|\mathbf{r}_{h_1}-\mathbf{r}_{h_2}|^2}}$, is

$$V^{(hh)n_1,n_2,n_3,n_4}_{j_1,j_2,j_3,j_4} = \int qdqd\theta\frac{2\pi e^2}{\epsilon q}\,\Xi^{(h)j_4,n_4,K,\downarrow}_{j_1,n_1,K,\downarrow}(\mathbf{q}) \times \Xi^{(h)j_3,n_3,K,\downarrow}_{j_2,n_2,K,\downarrow}(-\mathbf{q}).$$

1. Zero magnetic field

In the absence of a magnetic field, we initiate from Eq. (C3) to derive the Coulomb interaction matrix element. The derivation is concerned with function Ξ and can be numerically calculated by setting layer distance $d = 0$. By using the wave function without magnetic field in Eq. (B7), we have

$$\Xi^{(e)j_k,n_k,\tau_k,s_k}_{j_i,n_i,\tau_i,s_i}(\mathbf{q}) = M^{j_k,n_k,\tau_k,s_k}_{j_i,n_i,\tau_i,s_i}\int_0^{R_e} r_e dr_e \int_0^{2\pi} d\theta_e e^{i\mathbf{q}\cdot\mathbf{r_e}}\Big\{C^{j_k,n_k,\tau_k,s_k}_{j_i,n_i,\tau_i,s_i} e^{-i[(j_i-\frac{\tau_i}{2})-(j_k-\frac{\tau_k}{2})]\theta_e} J_{(j_i-\frac{\tau_i}{2})}\big(\sqrt{\kappa_{j_i,n_i,\tau_i,s_i}}r_e\big)J_{(j_k-\frac{\tau_k}{2})}\big(\sqrt{\kappa_{j_k,n_k,\tau_k,s_k}}r_e\big) + e^{-i[(j_i+\frac{\tau_i}{2})-(j_k+\frac{\tau_k}{2})]\theta_e} J_{(j_i+\frac{\tau_i}{2})}\big(\sqrt{\kappa_{j_i,n_i,\tau_i,s_i}}r_e\big)J_{(j_k+\frac{\tau_k}{2})}\big(\sqrt{\kappa_{j_k,n_k,\tau_k,s_k}}r_e\big)\Big\}, \tag{C5}$$

where we define

$$C^{j_k,n_k,\tau_k,s_k}_{j_i,n_i,\tau_i,s_i} = (2a_e t_e)^2 \frac{\sqrt{\kappa_{j_i,n_i,\tau_i,s_i}}}{2E_{s_i,\tau_i,n_i,j_i}-\Delta_e}\frac{\sqrt{\kappa_{j_k,n_k,\tau_k,s_k}}}{2E_{j_k,n_k,\tau_k,s_k}-\Delta_e}, \tag{C6}$$

$$M^{j_k,n_k,\tau_k,s_k}_{j_i,n_i,\tau_i,s_i} = N^*_{j_i,n_i,\tau_i,s_i}N_{j_k,n_k,\tau_k,s_k}\varrho_{j_i,\tau_i}\varrho_{j_k,\tau_k}, \tag{C7}$$

with a_e and t_e being the lattice constant and the hopping parameter of the electron layer, respectively. Subsequently, we acquire

$$\Xi^{(e)j_k,n_k,\tau_k,s_k}_{j_i,n_i,\tau_i,s_i}(\mathbf{q}) = M^{j_k,n_k,\tau_k,s_k}_{j_i,n_i,\tau_i,s_i}R_e^2\int_0^1 r'_e dr'_e\Big\{C^{j_k,n_k,\tau_k,s_k}_{j_i,n_i,\tau_i,s_i} i^{|(j_k-\frac{\tau_k}{2})-(j_i-\frac{\tau_i}{2})|}J_{|(j_k-\frac{\tau_k}{2})-(j_i-\frac{\tau_i}{2})|}(q_e r'_e)J_{(j_i-\frac{\tau_i}{2})}\big(K^e_i r'_e\big)J_{(j_k-\frac{\tau_k}{2})}\big(K^e_k r'_e\big) + i^{|(j_k+\frac{\tau_k}{2})-(j_i+\frac{\tau_i}{2})|}J_{|(j_k+\frac{\tau_k}{2})-(j_i+\frac{\tau_i}{2})|}(q_e r'_e)J_{(j_i+\frac{\tau_i}{2})}\big(K^e_i r'_e\big)J_{(j_k+\frac{\tau_k}{2})}\big(K^e_k r'_e\big)\Big\}, \tag{C8}$$

where we define $K^e_i = R_e\sqrt{\kappa_{j_i,n_i,\tau_i,s_i}}$, $K^e_k = R_e\sqrt{\kappa_{j_k,n_k,\tau_k,s_k}}$with dimensionless integral variables $q_e = R_e q$, $r'_e = \frac{r_e}{R_e}$. Similarly, we can obtain the function for the hole,

$$\Xi^{(h)J_k,N_k,T_k,S_k}_{J_i,N_i,T_i,S_i}(\mathbf{q}) = M^{J_k,N_k,T_k,S_k}_{J_i,N_i,T_i,S_i}R_h^2\int_0^1 r'_h dr'_h\Big\{C^{J_k,N_k,T_k,S_k}_{J_i,N_i,T_i,S_i} i^{|(J_k-\frac{T_k}{2})-(J_i-\frac{T_i}{2})|}J_{|(J_k-\frac{T_k}{2})-(J_i-\frac{T_i}{2})|}(-q_h r'_h)J_{(J_i-\frac{T_i}{2})}\big(K^h_i r'_h\big)J_{(j_k-\frac{\tau_k}{2})}\big(K^h_k r'_h\big) + i^{|(J_k+\frac{T_k}{2})-(J_i+\frac{T_i}{2})|}J_{|(J_k+\frac{T_k}{2})-(J_i+\frac{T_i}{2})|}(-q_h r'_h)J_{(J_i+\frac{T_i}{2})}\big(K^h_i r'_h\big)J_{(J_k+\frac{T_k}{2})}\big(K^h_k r'_h\big)\Big\}, \tag{C9}$$

with $K^h_i = R_h\sqrt{\kappa_{j_i,n_i,\tau_i,s_i}}$ and $q_h = R_h q$, $r'_h = \frac{r_h}{R_h}$. We need to choose appropriate dimensionless integral variables to improve the efficiency of the numerical integration.

2. With magnetic field

In the presence of a magnetic field, only the function Ξ needs to be modified. It is given by using the wave function in Eq. (B13),

$$\Xi^{(e)j_k,n_k,\tau_k,s_k}_{j_i,n_i,\tau_i,s_i}(\mathbf{q}) = N^*_{j_i,n_i,\tau_i,s_i}N_{j_k,n_k,\tau_k,s_k}a^e_L\int_0^1 dr'_e\big(a^e_L r'_e\big)^{|j_i-\frac{\tau_i}{2}|+|j_k-\frac{\tau_k}{2}|+1}\exp\big[-\beta_e\big(a^e_L r'_e\big)^2\big] \times\big\{i^{|(j_k-\frac{\tau_k}{2})-(j_i-\frac{\tau_i}{2})|}J_{|(j_k-\frac{\tau_k}{2})-(j_i-\frac{\tau_i}{2})|}(q_e r'_e){}_1F_1\big[\alpha_{j_i,n_i,\tau_i,s_i}, b_{j_i,\tau_i}, \beta_e\big(a^e_L r'_e\big)^2\big]{}_1F_1\big[\alpha_{j_k,n_k,\tau_k,s_k}, b_{j_k,\tau_k}, \beta_e\big(a^e_L r'_e\big)^2\big] + \gamma_{j_i,n_i,\tau_i,s_i}\gamma_{j_k,n_k,\tau_k,s_k} i^{|(j_k+\frac{\tau_k}{2})-(j_i+\frac{\tau_i}{2})|}\big(a^e_L r'_e\big)^{-2}J_{|(j_k+\frac{\tau_k}{2})-(j_i+\frac{\tau_i}{2})|}(q_e r'_e)\Gamma_{j_i,n_i,\tau_i,s_i}\big(a^e_L r'_e\big)\Gamma_{j_k,n_k,\tau_k,s_k}\big(a^e_L r'_e\big)\big\}, \tag{C10}$$

where we define $\frac{R_e}{a_e} = a^e_L$, $r'_e = \frac{r_e}{R_e}$, and $q_e = R_e q$. Here, the function $\Gamma(\rho)$ and γ are defined in Eq. (B13). Additionally, we expand upon the established definitions and, similarly, we can deduce $\Xi^{(h)j_k,n_k,\tau_k,s_k}_{j_i,n_i,\tau_i,s_i}$. Then all the Coulomb interaction matrix elements can be obtained.

[1] Y. Jiang, S. Chen, W. Zheng, B. Zheng, and A. Pan, Interlayer exciton formation, relaxation, and transport in TMD van der Waals heterostructures, Light Sci. Appl. **10**, 72 (2021).

[2] S. Latini, K. T. Winther, T. Olsen, and K. S. Thygesen, Interlayer excitons and band alignment in MoS_2/hBN/WSe_2 van der Waals heterostructures, Nano Lett. **17**, 938 (2017).

[3] S. Manzeli, D. Ovchinnikov, D. Pasquier, O. V. Yazyev, and A. Kis, 2D transition metal dichalcogenides, Nat. Rev. Mater. **2**, 17033 (2017).

[4] T. Mueller and E. Malic, Exciton physics and device application of two-dimensional transition metal dichalcogenide semiconductors, npj 2D Mater. Appl. **2**, 29 (2018).

[5] M. Xu, T. Liang, M. Shi, and H. Chen, Graphene-like two-dimensional materials, Chem. Rev. **113**, 3766 (2013).

[6] D. Xiao, G.-B. Liu, W. Feng, X. Xu, and W. Yao, Coupled spin and valley physics in monolayers of MoS_2 and other group-VI dichalcogenides, Phys. Rev. Lett. **108**, 196802 (2012).

[7] A. Kormányos, G. Burkard, M. Gmitra, J. Fabian, V. Zólyomi, N. D. Drummond, and V. Fal'ko, kp theory for two-dimensional transition metal dichalcogenide semiconductors, 2D Mater. **2**, 022001 (2015).

[8] A. K. Geim and I. V. Grigorieva, Van der Waals heterostructures, Nature (London) **499**, 419 (2013).

[9] M. Z. Bellus, M. Li, S. D. Lane, F. Ceballos, Q. Cui, X. C. Zeng, and H. Zhao, Type-I van der Waals heterostructure formed by MoS_2 and ReS_2 monolayers, Nanoscale Horiz. **2**, 31 (2017).

[10] J. Kang, S. Tongay, J. Zhou, J. Li, and J. Wu, Band offsets and heterostructures of two-dimensional semiconductors, Appl. Phys. Lett **102**, 012111 (2013).

[11] D. Unuchek, A. Ciarrocnanotechi, A. Avsar, Z. Sun, K. Watanabe, T. Taniguchi, and A. Kis, Valley-polarized exciton currents in a van der Waals heterostructure, Nat. Nanotechnol. **14**, 1104 (2019).

[12] Y. Hajati, M. Alipouzadeh, D. Schulz, and J. Berakdar, Tuning layer-, perfect-spin-, and valley-polarized transport in transition-metal-dichalcogenide bilayer junctions, Phys. Rev. Appl. **20**, 024075 (2023).

[13] Y. Zhao, L. Du, S. Yang, J. Tian, X. Li, C. Shen, J. Tang, Y. Chu, K. Watanabe, T. Taniguchi *et al.*, Interlayer exciton complexes in bilayer MoS_2, Phys. Rev. B **105**, L041411 (2022).

[14] A. S. Rodin and A. H. Castro Neto, Excitonic collapse in semiconducting transition-metal dichalcogenides, Phys. Rev. B **88**, 195437 (2013).

[15] Y. N. Gartstein, X. Li, and C. Zhang, Exciton polaritons in transition-metal dichalcogenides and their direct excitation via energy transfer, Phys. Rev. B **92**, 075445 (2015).

[16] M. Van der Donck and F. M. Peeters, Interlayer excitons in transition metal dichalcogenide heterostructures, Phys. Rev. B **98**, 115104 (2018).

[17] S. Wu, L. Cheng, and Q. Wang, Exciton states and absorption spectra in freestanding monolayer transition metal dichalcogenides: A variationally optimized diagonalization method, Phys. Rev. B **100**, 115430 (2019).

[18] L. G. M. Tenório, T. A. S. Pereira, K. Mohseni, T. Frederico, M. R. Hadizadeh, D. R. da Costa, and A. J. Chaves, Tunable properties of excitons in double monolayer semiconductor heterostructures, Phys. Rev. B **108**, 035421 (2023).

[19] J.-J. Su and A. MacDonald, How to make a bilayer exciton condensate flow, Nat. Phys. **4**, 799 (2008).

[20] D. D. Dai and L. Fu, Strong-coupling phases of trions and excitons in electron-hole bilayers at commensurate densities, Phys. Rev. Lett. **132**, 196202 (2024).

[21] O. L. Berman and R. Y. Kezerashvili, Superfluidity of dipolar excitons in a transition metal dichalcogenide double layer, Phys. Rev. B **96**, 094502 (2017).

[22] M. A. Semina, M. M. Glazov, and E. Sherman, Interlayer exciton–polaron in atomically thin semiconductors, Ann. Phys. Berlin **532**, 2000339 (2020).

[23] Z. A. Iakovlev, M. A. Semina, M. M. Glazov, and E. Y. Sherman, Flexural deformations and collapse of bilayer two-dimensional crystals by interlayer excitons, Phys. Rev. B **105**, 205305 (2022).

[24] P. Soubelet, A. Delhomme, A. V. Stier, and J. J. Finley, Polarons shape the interlayer exciton emission of $\mathrm{MoSe}_2/\mathrm{WSe}_2$ heterobilayers, arXiv:2407.15649.

[25] A. Abouelkomsan, E. J. Bergholtz, and S. Chatterjee, Multiferroicity and topology in twisted transition metal dichalcogenides, Phys. Rev. Lett. **133**, 026801 (2024).

[26] X. Yang, S. Zhang, Z. Zhang, J. Lin, X. Liu, Z. Huang, L. Zhang, W. Luo, J. He, and X. Yuan, Controlled fabrication of $\mathrm{CsPbI}_2\mathrm{Br}$/transition metal dichalcogenide van der Waals heterostructure with fast carrier transfer process and interlayer exciton formation, Physica E **153**, 115788 (2023).

[27] M. Chen, R. Chang, X. Yang, C. Lu, S. Zhang, Z. Zhang, J. He, and X. Yuan, Van der Waals epitaxy of $\mathrm{CsPbBr}_3/\mathrm{WSe}_2$ heterostructure and dynamics study of exciton recombination, J. Phys. D **57**, 235103 (2024).

[28] C. Lu, S. Zhang, M. Chen, H. Chen, M. Zhu, Z. Zhang, J. He, L. Zhang, and X. Yuan, Van der Waals epitaxy of type-II band alignment CsPbI_3/TMDC heterostructure for optoelectronic applications, Front. Phys. **19**, 53206 (2024).

[29] T. Chakraborty, *Quantum Dots* (North-Holland, Amsterdam, 1999).

[30] T. Chakraborty, Nanoscopic quantum rings: A new perspective, Adv. Sol. State Phy. **43**, 79 (2003).

[31] T. Chakraborty, A. K. Manaselyan, and M. G. Barseghyan, Electronic, magnetic and optical properties of quantum rings in novel systems, in *Physics of Quantum Rings*, edited by V. M. Fomin (Springer, Cham, 2018), pp. 283–326.

[32] H.-Y. Chen, V. Apalkov, and T. Chakraborty, Fock-Darwin states of Dirac electrons in graphene-based artificial atoms, Phys. Rev. Lett. **98**, 186803 (2007).

[33] V. Halonen, T. Chakraborty, and P. Pietiläinen, Excitons in a parabolic quantum dot in magnetic fields, Phys. Rev. B **45**, 5980 (1992).

[34] A. Zrenner, L. V. Butov, M. Hagn, G. Abstreiter, G. Böhm, and G. Weimann, Quantum dots formed by interface fluctuations in AlAs/GaAs coupled quantum well structures, Phys. Rev. Lett. **72**, 3382 (1994).

[35] Y. Zeng and A. H. MacDonald, Strong modulation limit of excitons and trions in moiré materials, Phys. Rev. B **106**, 035115 (2022).

[36] M. Zarenia, B. Partoens, T. Chakraborty, and F. M. Peeters, Electron-electron interactions in bilayer graphene quantum dots, Phys. Rev. B **88**, 245432 (2013).

[37] F.-M. Jing, Z.-Z. Zhang, G.-Q. Qin, G. Luo, G. Cao, H.-O. Li, X.-X. Song, and G.-P. Guo, Gate-controlled quantum dots based on 2D materials, Adv. Quantum Technol. **5**, 2100162 (2022).

[38] Z. Wang, Y. Yuan, X. Liu, J. Sun, M. Muruganathan, and H. Mizuta, Quantum dot formation in controllably doped graphene nanoribbon, ACS Nano **13**, 7502 (2019).

[39] Z. Wang, Y. Yuan, X. Liu, M. Muruganathan, H. Mizuta, and J. Sun, Double quantum dot-like transport in controllably doped graphene nanoribbon, Appl. Phys. Lett **118**, 083105 (2021).

[40] Y. Guo, C.-C. Shu, D. Dong, and F. Nori, Vanishing and revival of resonance Raman scattering, Phys. Rev. Lett. **123**, 223202 (2019).

[41] C. Shou, Q. Zhang, W. Luo, and G. Huang, Photon storage and routing in quantum dots with spin-orbit coupling, Opt. Express **29**, 9772 (2021).

[42] M. Mirzakhani, M. Zarenia, D. R. da Costa, S. A. Ketabi, and F. M. Peeters, Energy levels of abc-stacked trilayer graphene quantum dots with infinite-mass boundary conditions, Phys. Rev. B **94**, 165423 (2016).

[43] A. Kormányos, V. Zólyomi, N. D. Drummond, and G. Burkard, Spin-orbit coupling, quantum dots, and qubits in monolayer transition metal dichalcogenides, Phys. Rev. X **4**, 011034 (2014).

[44] G.-B. Liu, H. Pang, Y. Yao, and W. Yao, Intervalley coupling by quantum dot confinement potentials in monolayer transition metal dichalcogenides, New J. Phys. **16**, 105011 (2014).

[45] F. Qu, A. Dias, J. Fu, L. Villegas-Lelovsky, and D. L. Azevedo, Tunable spin and valley dependent magneto-optical absorption

in molybdenum disulfide quantum dots, Sci. Rep. **7**, 41044 (2017).

[46] A. C. Dias, J. Fu, L. Villegas-Lelovsky, and F. Qu, Robust effective Zeeman energy in monolayer MoS_2 quantum dots, J. Phys.: Condens. Matter **28**, 375803 (2016).

[47] D. Miravet, A. Altıntaş, A. W. Rodrigues, M. Bieniek, M. Korkusinski, and P. Hawrylak, Interacting holes in gated WSe_2 quantum dots, Phys. Rev. B **108**, 195407 (2023).

[48] A. Mitra, A. J. Zafar, and V. Apalkov, Ultrafast field-driven valley polarization of transition metal dichalcogenide quantum dots, J. Phys.: Condens. Matter **36**, 205302 (2024).

[49] A. Mitra, A. J. Zafar, S. J. Hosseini, and V. Apalkov, Ultrafast high harmonic generation in transition metal dichalcogenide quantum dots, Phys. Rev. B **109**, 155425 (2024).

[50] S.-Y. Chen, Z. Lu, T. Goldstein, J. Tong, A. Chaves, J. Kunstmann, L. Cavalcante, T. Wozniak, G. Seifert, D. Reichman *et al.*, Luminescent emission of excited Rydberg excitons from monolayer WSe_2, Nano Lett. **19**, 2464 (2019).

[51] C. Yannouleas and U. Landman, Quantum Wigner molecules in moiré materials, Phys. Rev. B **108**, L121411 (2023).

[52] C. Zerba, C. Kuhlenkamp, A. Imamoğlu, and M. Knap, Realizing topological superconductivity in tunable Bose-Fermi mixtures with transition metal dichalcogenide heterostructures, Phys. Rev. Lett. **133**, 056902 (2024).

[53] J. Li, Y. Zhong, and D. Zhang, Excitons in monolayer transition metal dichalcogenides, J. Phys.: Condens. Matter **27**, 315301 (2015).

[54] D. Luo, A. P. Reddy, T. Devakul, and L. Fu, Artificial intelligence for artificial materials: Moiré atom, arXiv:2303.08162.

[55] M. V. Berry and R. Mondragon, Neutrino billiards: Time-reversal symmetry-breaking without magnetic fields, Proc. R. Soc. London A **412**, 53 (1987).

[56] M. Grujić, M. Zarenia, A. Chaves, M. Tadić, G. A. Farias, and F. M. Peeters, Electronic and optical properties of a circular graphene quantum dot in a magnetic field: Influence of the boundary conditions, Phys. Rev. B **84**, 205441 (2011).

[57] T. Paananen and R. Egger, Finite-size version of the excitonic instability in graphene quantum dots, Phys. Rev. B **84**, 155456 (2011).

[58] T. Paananen, R. Egger, and H. Siedentop, Signatures of Wigner molecule formation in interacting Dirac fermion quantum dots, Phys. Rev. B **83**, 085409 (2011).

[59] V. Raca and M. V. Milovanović, Excitonic physics in a Dirac quantum dot, Phys. Rev. B **96**, 195434 (2017).

[60] Y. Zhou, C. Li, Y. Zhang, L. Wang, X. Fan, L. Zou, Z. Cai, J. Jiang, S. Zhou, B. Zhang *et al.*, Controllable thermochemical generation of active defects in the horizontal/vertical MoS_2 for enhanced hydrogen evolution, Adv. Funct. Mater. **33**, 2304302 (2023).

[61] W. Chu, X. Zhou, Z. Wang, X. Fan, X. Guo, C. Li, J. Yue, F. Ouyang, J. Zhao, and Y. Zhou, Stable alkali halide vapor assisted chemical vapor deposition of 2D $HfSe_2$ templates and controllable oxidation of its heterostructures, Front. Phys. **19**, 33212 (2024).

[62] D. H. Keum, S. Cho, J. H. Kim, D.-H. Choe, H.-J. Sung, M. Kan, H. Kang, J.-Y. Hwang, S. W. Kim, H. Yang *et al.*, Band gap opening in few-layered monoclinic $MoTe_2$, Nat. Phys. **11**, 482 (2015).

[63] S. Tongay, H. Sahin, C. Ko, A. Luce, W. Fan, K. Liu, J. Zhou, Y.-S. Huang, C.-H. Ho, J. Yan *et al.*, Monolayer behaviour in bulk ReS_2 due to electronic and vibrational decoupling, Nat. Commun. **5**, 3252 (2014).

[64] P. V. Nguyen, N. C. Teutsch, N. P. Wilson, J. Kahn, X. Xia, A. J. Graham, V. Kandyba, A. Giampietri, A. Barinov, G. C. Constantinescu *et al.*, Visualizing electrostatic gating effects in two-dimensional heterostructures, Nature (London) **572**, 220 (2019).

[65] P. Pietiläinen and T. Chakraborty, Energy levels and magneto-optical transitions in parabolic quantum dots with spin-orbit coupling, Phys. Rev. B **73**, 155315 (2006).

[66] R. Wang, T. A. Sedrakyan, B. Wang, L. Du, and R.-R. Du, Excitonic topological order in imbalanced electron-hole bilayers, Nature (London) **619**, 57 (2023).

[67] L. C. Camenzind, L. Yu, P. Stano, J. D. Zimmerman, A. C. Gossard, D. Loss, and D. M. Zumbühl, Spectroscopy of quantum dot orbitals with in-plane magnetic fields, Phys. Rev. Lett. **122**, 207701 (2019).

[68] W. Luo, S. Peng, and T. Chakraborty, Spin textures in quantum dots and quantum rings, in *Encyclopedia of Condensed Matter Physics*, 2nd ed., edited by T. Chakraborty (Academic Press, Oxford, 2024), pp. 400–414.

[69] W. Luo and T. Chakraborty, Tuning the topological features of quantum-dot hydrogen and helium by a magnetic field, Phys. Rev. B **100**, 085309 (2019).

[70] P. A. Maksym and T. Chakraborty, Quantum dots in a magnetic field: Role of electron-electron interactions, Phys. Rev. Lett. **65**, 108 (1990).

[71] S. Avetisyan, P. Pietiläinen, and T. Chakraborty, Strong enhancement of Rashba spin-orbit coupling with increasing anisotropy in the Fock-Darwin states of a quantum dot, Phys. Rev. B **85**, 153301 (2012).

[72] S. Avetisyan, P. Pietiläinen, and T. Chakraborty, Superintense highly anisotropic optical transitions in anisotropic quantum dots, Phys. Rev. B **88**, 205310 (2013).

[73] T. Chakraborty, A. Manaselyan, M. Barseghyan, and D. Laroze, Controllable continuous evolution of electronic states in a single quantum ring, Phys. Rev. B **97**, 041304(R) (2018).

[74] D. A. Ruiz-Tijerina, I. Soltero, and F. Mireles, Theory of moiré localized excitons in transition metal dichalcogenide heterobilayers, Phys. Rev. B **102**, 195403 (2020).

[75] J. Keski-Rahkonen, A. Ruhanen, E. J. Heller, and E. Räsänen, Quantum lissajous scars, Phys. Rev. Lett. **123**, 214101 (2019).